the magnitude of the gain. Thus, the delay time of ~0.5 s observed in Fig. 4 increases to 12 s at $E_o = 46$ V/µm. Furthermore, the use of additional polymer layers will not decrease the threshold for oscillation noticeably unless an index-matching liquid is used to reduce the reflection losses accordingly. Once oscillation has been achieved, however, the PC reflectivity will increase significantly faster with E_o for a larger multilayer stack. Finally, predicting the threshold for oscillation or the value of R from measurements of two-beam coupling gain is not a simple matter. Recent work has shown that these polymers benefit from gain enhancement due to very slow motion of the index grating, which means that the cavity beam is expected to be frequency-shifted from the pumping beam. This complicates the theoretical analysis to a level beyond the scope of this report (25).

REFERENCES AND NOTES

1. P. Günter and J.-P. Huignard, Eds., *Photorefractive Materials and Their Applications I & II* (Springer-Verlag, Berlin, 1988 and 1989); P. Yeh, *Introduction to Photorefractive Nonlinear Optics* (Wiley, New York, 1993).
2. L. Solymar, D. J. Webb, A. Grunnet-Jepsen, *The Physics and Applications of Photorefractive Materials* (Oxford Univ. Press, New York, 1996).
3. S. Ducharme, J. C. Scott, R. J. Twieg, W. E. Moerner, *Phys. Rev. Lett.* **66**, 1846 (1991).
4. K. Meerholz, B. L. Volodin, Sandalphon, B. Kippelen, N. Peyghambarian, *Nature* **371**, 497 (1994).
5. M. Liphardt *et al.*, *Science* **263**, 367 (1994); P. M. Lundquist *et al.*, *ibid.* **274**, 1182 (1996); G. P. Wiederrecht, B. A. Yoon, M. R. Wasielewski, *ibid.* **270**, 1794 (1995).
6. W. E. Moerner, A. Grunnet-Jepsen, C. L. Thompson, *Annu. Rev. Mater. Sci.* **27**, 585 (1997).
7. W. E. Moerner and S. M. Silence, *Chem. Rev.* **94**, 127 (1994).
8. S. M. Silence, C. A. Walsh, J. C. Scott, W. E. Moerner, *Appl. Phys. Lett.* **61**, 2967 (1992).
9. A. Grunnet-Jepsen, C. L. Thompson, R. J. Twieg, W. E. Moerner, *ibid.* **70**, 1515 (1997).
10. L. Yu, W. K. Chan, Z. Peng, A. Gharavi, *Acc. Chem. Res.* **29**, 13 (1996).
11. J. P. Huignard and A. Marrakchi, *Opt. Commun.* **38**, 249 (1981).
12. D. Z. Anderson, D. M. Lininger, J. Feinberg, *Opt. Lett.* **12**, 123 (1987); D. M. Lininger, P. J. Martin, D. Z. Anderson, *ibid.* **14**, 697 (1989); D. Z. Anderson, C. Benkert, B. Chorbajian, A. Hermanns, *ibid.* **16**, 250 (1991); A. A. Zozulya, M. Saffman, D. Z. Anderson, *Phys. Rev. Lett.* **73**, 818 (1994).
13. A related effect, beam fanning, has also been observed in our materials and is reported separately (A. Grunnet-Jepsen, C. L. Thompson, R. J. Twieg, W. E. Moerner, *J. Opt. Soc. Am. B*, in press).
14. A. P. Yakimovich, *Opt. Spectrosc.* **49**, 85 (1980); A. R. Tanguay and R. V. Johnson, *J. Opt. Soc. Am. A.* **3**, P53 (1986); G. P. Nordin, R. V. Johnson, A. R. Tanguay, *ibid.* **9**, 2206 (1992).
15. J. J. Stankus, S. M. Silence, W. E. Moerner, G. C. Bjorklund, *Opt. Lett.* **19**, 1480 (1994); R. de Vré and L. Hesselink, *J. Opt. Soc. Am. B.* **11**, 1800 (1994).
16. The theoretical fits were obtained by fitting the standard PR theory (17) to the single-layer sample (solid line) as detailed in (9) and calculating the gain according to $g_2 = \exp(2\Gamma L)$ (dotted line) and $g_3 = \exp(3\Gamma L)$ (dashed line).
17. N. V. Kukhtarev, V. B. Markov, S. G. Odulov, M. S. Soskin, V. L. Vinetskii, *Ferroelectrics* **22**, 949 (1979).
18. D. Gabor, *Proc. R. Soc. London Ser. A*, **197**, 454 (1949).
19. H. Kogelnik, *Bell Syst. Tech. J.* **44**, 2451 (1965).
20. R. A. Fisher, Ed., *Optical Phase Conjugation* (Academic Press, New York, 1983).
21. B. Ya. Zel'dovich, V. I. Popovichev, V. V. Raguel'sky, F. S. Faizullov, *Sov. Phys. JETP* **15**, 109 (1972).
22. R. W. Hellwarth, *J. Opt. Soc. Am.* **67**, 1 (1977).
23. J. Feinberg and R. W. Hellwarth, *Opt. Lett.* **5**, 519 (1980); J. O. White, M. Cronin-Golomb, B. Fischer, A. Yariv, *Appl. Phys. Lett.* **40**, 450 (1982); J. Feinberg, *Opt. Lett.* **7**, 486 (1982); M. Cronin-Golomb, J. O. White, B. Fischer, A. Yariv, *ibid.*, p. 313; M. Cronin-Golomb, B. Fischer, J. Nilsen, J. O. White, A. Yariv, *Appl. Phys. Lett.* **41**, 219 (1982); M. Cronin-Golomb, B. Fischer, J. O. White, A. Yariv, *ibid.*, p. 689; *IEEE J. Quantum Electron.* **20**, 12 (1984).
24. J. E. Millerd, E. M. Garmire, M. B. Klein, *J. Opt. Soc. Am. B.* **9**, 1499 (1992).
25. V. A. Kalinin and L. Solymar, *Appl. Phys. B.* **45**, 129 (1988).
26. We acknowledge R. J. Twieg for supplying the PDCST chromophore and the U.S. Air Force Office of Scientific Research grant F49620-96-1-0135 for partial support of this work.

20 March 1997; accepted 6 May 1997

Formation of a Silicate L_3 Phase with Continuously Adjustable Pore Sizes

K. M. McGrath, D. M. Dabbs, N. Yao, I. A. Aksay, S. M. Gruner*

The lyotropic L_3 phase was used as a template to form nanoporous monolithic silicates with continuously adjustable pore sizes. The monolith was optically isotropic and transparent with a nonperiodic network. The pore size was adjusted by a change in the solvent volume fraction rather than by a change of the surfactant. Unlike other silicates, the bicontinuous pores were water-filled; removal of surfactant was not necessary to access the pores. Measured characteristic dimensions were from six to more than 35 nanometers. For a given solvent fraction, x-ray scattering indicated little variation of pore widths, in marked contrast to the polydisperse pores of aerogels.

Since the demonstration that surfactants could be used in the fabrication of silica mesophases (1), amphiphiles have been used to produce inorganic materials with a variety of mesomorphic structures, including lamellar, hexagonally packed tubular, and cubic forms (2–12). Surfactant-induced assembly of inorganic structures is now recognized as a way to make novel nanoporous materials with larger pore sizes than was previously possible. However, techniques developed thus far have limited capability to produce very large pores of a predetermined size. Here we describe the synthesis and characterization of a new, random, bicontinuous silicate mesomorph for which predetermined pore sizes, over a very large size range, may be obtained.

Most procedures for forming mesoporous silicates rely on the micelle-forming properties of a surfactant, typically at a low surfactant concentration. The addition of an inorganic precursor, such as an alkoxysilane, leads to association and co-assembly into a mesophase precipitant whose structural dimensions are con-

trolled by the surfactant length. Polymerization of the inorganic precursor and removal of the surfactant results in a rigid silica shell conforming to the structural shape of the mesophase. However, the use of dilute surfactant solutions limits the ability to predict the topology of the mesophase. Also, the typical product of the process is a powder of micrometer-sized particles, thereby limiting uses in filtration, optical, or electronic applications, where large-area thin films or large uniform monoliths of material are required. Finally, the pore volume is filled with surfactant; that is, the surfactant must be removed before the pores can be accessed.

These difficulties may be partially avoided by the use of high-concentration surfactant systems in which either the inorganic precursors minimally perturb a preexisting surfactant-water liquid crystalline (LC) structure or the LC nature of the system may be recovered under appropriate experimental conditions, as shown by Attard *et al.* (6). Also, because the inorganic precursor does not precipitate out of solution, the resultant material conforms to the shape of the container in which it forms, thereby allowing fabrication of large monoliths of a desired size and shape. However, even in these cases, the pore size is limited by the surfactant and the limited range of compositions on the phase diagram for a given mesomorphic structure.

Applications of silicate mesophases as filtration media, optical materials, and nanocomposites would be facilitated if the

K. M. McGrath and S. M. Gruner, Department of Physics and Princeton Materials Institute, Princeton University, Bowen Hall, 70 Prospect Avenue, Post Office Box 708, Princeton, NJ 08544, USA.
D. M. Dabbs and I. A. Aksay, Department of Chemical Engineering and Princeton Materials Institute, Princeton University, Princeton, NJ 08544, USA.
N. Yao, Princeton Materials Institute, Princeton University, Princeton, NJ 08544, USA.

*To whom correspondence should be addressed: Physics Department, Cornell University, Clark Hall, Ithaca, NY 14853–2501.

pore dimensions could be readily controlled over a wide range of sizes, if a continuous network of pores permeated throughout large monoliths of material of a desired shape and size, and if it were not necessary to remove the surfactant to access the pores. Here, we describe the synthesis and characterization of a surfactant-silica mesophase with these desirable properties. It is based on the surfactant L_3 phase (Fig. 1) (13–19) and has the advantage of forming arbitrarily large, water-clear silicate monoliths that contain a random, bicontinuous pore structure. Very large pores may be obtained, because the pore size is determined by the relative concentration of the constituents rather than the surfactant length. As opposed to closely related silica xerogels and aerogels, there is little variation in the width of the pores. The three-dimensional (3D) nature of the continuously connected pore networks also presents advantages because the pore structure is accessible from any external surface. In contrast, hexagonal pore networks typically align parallel to surfaces, which limits their use in thin films as filters.

The amphiphilic L_3 phase was first observed experimentally in the early 1980s and represented a new class of self-assembly for surfactant-water systems. The phase is optically isotropic and consists of a random network of a multiply connected bilayer that divides the water into two subvolumes (Fig. 1). The average water pore size may be readily varied over a very large range by changes in the relative ratios of the water and nonpolar constituents. The structure has been linked to the more common lamellar and cubic phases: The transition from the cubic to the L_3 phase may be thought of as a 3D isotropic randomization of the phase, while it maintains its bicontinuity, negative Gaussian curvature, and

equal subdivision of water. The lamellar-to-L_3 transition is a random formation of pores and necks such that the positioning of these defects produces an optically isotropic structure. The low viscosity (~6 mPa·s) and bicontinuity of the L_3 phase make it an ideal template for the formation of silicates.

We used a cetylpyridinium chloride (CpCl) surfactant system that has a well-characterized L_3 phase (13, 17, 20). The original quasi-ternary system consisted of CpCl with a cosurfactant, hexanol, in brine (1 weight % NaCl in water). The nature of the head group of CpCl is such that the important ion of the added salt for electrostatic shielding is the chloride ion; as such, the phase behavior of the system will not change significantly by the replacement of NaCl with HCl at the same concentration. We prepared samples by weighing out CpCl and adding the appropriate amount of hexanol and HCl solution. Solutions were prepared with a CpCl-to-hexanol ratio of 1.15 and with aqueous solvent weight fractions from 55 to 95%. The solvent had an initial pH of 0.7, yielding final solutions of extremely low pH; small visual variances in the samples were due solely to varying solvent composition. The L_3 phase formed readily for each sample, achieving equilibrium in no more than 2 days.

Tetramethoxysilane (TMOS) was added to the equilibrated L_3 phases at a fixed mole ratio of 1:4 to the HCl solution. Hydrolysis was rapid and the TMOS was observed to mix readily to form a clear solution. The reaction evolved considerable heat. Once hydrolysis was complete (which was taken as the point at which the temperature had returned to room temperature), sealed samples were placed in an oven at 60°C and allowed to gel (condense).

Gelation times varied from 2 to 5 hours, with the shorter times for solutions containing less solvent. Gelled samples were transparent, optically isotropic, and colorless and

conformed to the shape of the vial. Samples were cured at 60°C for 1 week, during which time the strength of the resulting material was observed to increase, as tested by the resistance of the gel to fracture when pressure was applied with a spatula. The strength of the material varied with the condensation, with samples prepared at room temperature being much weaker than those synthesized at 60°C; this was attributed to lower cross-linking at the lower temperature. Also, variation in curing time produced materials of differing strengths, which are again due to increased cross-linking with longer cures. Throughout curing, samples remained transparent and optically isotropic and no precipitation was observed, which resulted in large monoliths of material. Sizes varied from 1 to ~400 mm³. No care was taken to control cracking after gelation. All final materials were air-dried at room temperature.

The characteristic dimensions (an average over the thickness of the bilayer plus the channel occupied by solvent) of the L_3 phases were determined by means of small-angle x-ray scattering (SAXS) at 20°C. Diffraction of a typical L_3 phase before polymerization gave a broad peak, with an intensity that scaled asymptotically as q^{-2} at a high q vector ($q = 4\pi \sin \theta/1.54$ Å, where 2θ is the angle between the incident and scattered beam directions), as expected for a local bilayer structure (Fig. 3). The existence of the peak indicates that the material has a well-defined characteristic spacing. The broadness of the peak is in part because of the random pore structure; that is, it results from the ensemble average of chord lengths that vary in size because they strike across the pores at random.

The dilution law for this phase, as determined by SAXS, is shown in Fig. 2. The phase follows a universal dilution law, which means that the characteristic distance in the system varies linearly with the
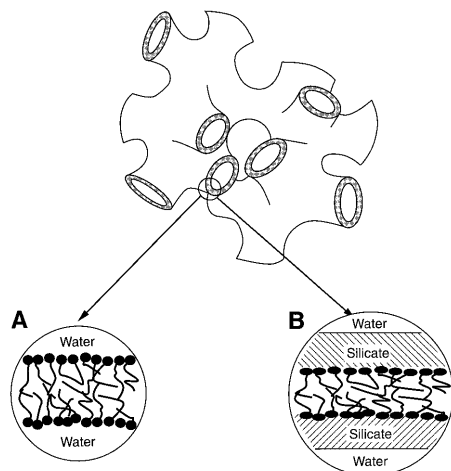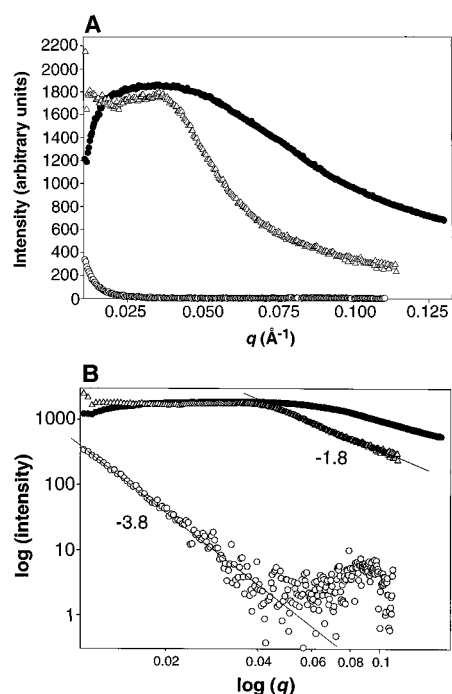

Fig. 1. Schematic representation of (**A**) the surfactant L_3 phase and (**B**) the silicate L_3.

Fig. 2. Dilution law (characteristic distance as a function of the solvent volume fraction φ) for the original L_3 phase (●), silicate L_3 (O), and scaled silicate L_3 (△; scaled with respect to increased total volume due to addition of the alkoxysilane and subsequent hyrolysis). The dimensions of the L_3 phases were determined from SAXS at 20°C. Data were obtained with a Rigaku (Tokyo, Japan) RU-200 rotating anode x-ray generator equipped with a microfocus cup. The generated Cu Kα x-rays were focused with bent mirror optics. Two-dimensional x-ray images were collected with a home-built charge-coupled device (CCD) detector based on a Thomson 512 by 512 pixel CCD (29). The digital powder diffraction images were azimuthally integrated along an arc of ±89.9° from the meridional axis to generate plots of scattered intensity versus $q = 4\pi \sin \theta/1.54$ Å, where 2θ is the angle between the incident and scattered beam directions. Samples were flame-sealed in glass x-ray capillaries 1.5 mm in diameter. The maximum characteristic spacing that could be measured was 35 nm; for larger spacings, the desired peak could not be resolved from the specimen and camera scatter near the beam stop.
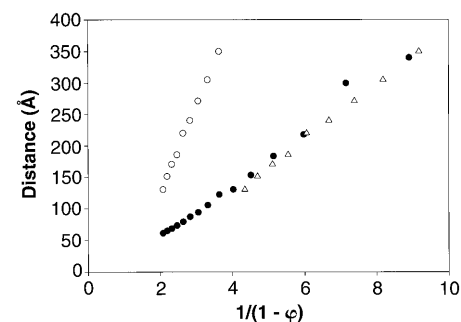
inverse of the volume fraction of amphiphile contained within the sample. The L_3 and lamellar phases are the only two known LC phases that follow such a law by which the topology of the phase remains unaltered over the entirety of the volume fraction for which the law is upheld. The measured characteristic distances ranged from 6 to 34 nm for solvent concentrations of 55 to 90 weight %, respectively. Characteristic distances greater than this could not be measured with the current apparatus, but previous studies at synchrotron sources on the L_3 phase of the system with NaCl have shown that the phase may be swollen extensively to concentrations approaching 100% solvent by weight, corresponding to distances on the order of 100 nm (13). This also appears to be the case here, as solutions showed no sign of phase sepa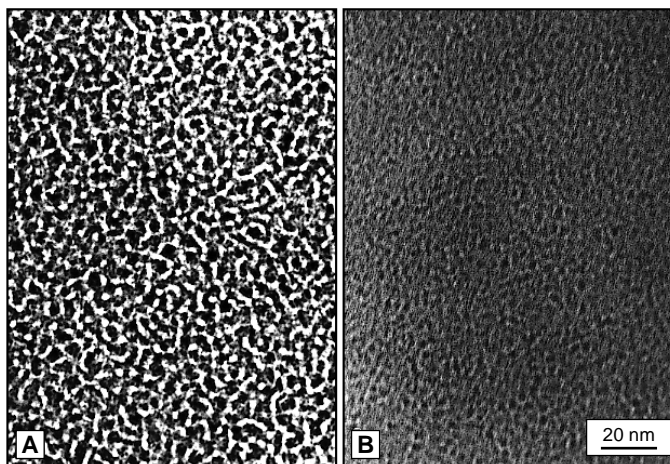ration upon further dilution (although the resultant solutions were beyond the measurement range of our apparatus); hence, characteristic distances ranging from 5 to 100 nm should be obtainable for the mesoporous silicates formed.

The results obtained for the samples after polymerization are also shown in Fig. 2. Despite the characteristic dimensions being displaced with respect to the original L_3 phases, the measured characteristic distances also follow a universal dilution law. As stated above, only L_3 phases are known to be optically isotropic and to follow such a dilution law by which the topology remains unaltered upon dilution. The diffraction patterns of the silicate materials closely resembled those of the amphiphilic L_3 phases, although in general, the SAXS signal was significantly increased for a comparable attenuation of the x-ray beam (because of scattering off the amorphous silica walls), and the characteristic peak was diminished and broader (because of the silica walls providing a region of contrast in addition to the surfactant bilayer).

The discrepancy in the dilution behavior for the two L_3 materials (Fig. 2) can be explained by the volume required by the silica precursor and methanol generated upon hydrolysis. On addition of the alkoxysilane to the L_3 phase, the volume was increased by an additional 116% in the case of an initially 55 weight % sample and 200% for a 95 weight % sample. This change pushed the nonsurfactant fraction of the samples to 79 and 98 weight %, respectively. Hence, if the alkoxysilane is merely a component of the solvent and does not fundamentally alter the nature of the structure (that is, the topology), its addition acts only to dilute the phase, shifting the measured characteristic spacing appropriately according to the measured universal scaling law. The measured characteristic spacings of the silicate L_3 materials that we replotted taking into account this dilution are shown in Fig. 2. The data now fall on top of the dilution curve obtained from the amphiphilic L_3 phases, indicating that dilution is the major consequence of the alkoxysilane addition. Note that hydrolysis of the TMOS results in the production of substantial quantities of methanol, which may be thought of as another spectator dilutent of the aqueous phase. Phase stability demands that the silane-diluted water and the methanol-diluted water both lie in the stable L_3 phase region of the phase diagram for the given amount of surfactant and hexanol. As such, a silicate L_3 phase was produced from a sample with initially 40% solvent by weight, despite the system not being in the L_3 phase region at this weight percentage. On the addition of the precursor alkoxysilane, the sample was shifted to 67 weight % solvent, which is within the L_3 phase regime.

An idealized figure of the L_3 silicate (Fig. 1B) shows the silica draped over the surfactant head group surface, displacing a characteristic volume of the solvent from each bilayer. The scaled plot of Fig. 2 suggests that the silica wall and surfactant thickness do not vary upon dilution. An estimate of the thickness of the solvent domains may be determined from the SAXS data if the thicknesses of the surfactant bilayer and the silica walls are known. The thickness of the bilayer is ~3 nm and does not change with concentration (20). Although a comprehensive study of the silica wall thickness has not been performed in silicate mesophases formed in acidic media, silicates formed in basic media have an estimated thickness on the order of >1 nm (21). If the thickness of the walls is comparable for the pH range used here, solvent channels initially wider than 2 nm would, after completion of condensation, still contain free solvent. Hence, for a characteristic spacing of 130 Å (55 weight % sample), a pore dimension of <80 Å is expected, which correlates reasonably

Fig. 3. (**A**) One-dimensional x-ray diffraction powder patterns of a silicate L_3 ($\triangle$; 55 weight % sample with characteristic spacing of 130 Å), amphiphilic L_3 ($\triangle$; 80 weight % sample with characteristic spacing of 153 Å), and a xerogel (O). Note that the concentration of the amphiphilic L_3 sample is close to the concentration of the silicate L_3 if one takes into account the dilution factor arising from the addition of alkoxysiliane and the subsequent methanol production (see text and Fig. 2). The silicate L_3 and amphiphilic L_3 patterns have been normalized to each other for ease of comparison. (**B**) The corresponding log-log plot from which the azimuthal behavior may be determined. For the xerogel, the intensity falls off as $q^{-3.8}$ and the amphiphilic L_3 falls off as $q^{-1.8}$. The high-q asymptote for the silicate L_3 could not be determined because of the limited q range of the data.

Fig. 4. TEM micrographs of (**A**) a 55 weight % silicate L_3 and (**B**) a xerogel of comparable density. Micrographs were obtained in a Philips (Mahwah, New Jersey) CM 200 Field-Emission-Gun TEM operated at 120 keV. The TEM images were acquired at both ambient and liquid nitrogen temperature; no visible variations in crystal structure were found at the two temperatures.

well with that measured from transmission electron microscopy (TEM) (see Fig. 4).

TMOS will also hydrolyze in the absence of surfactant; indeed, this is a recipe for making classic silica xerogels (*22–27*). In order to compare the silicate L_3 to xerogel materials, samples were made with the use of acidified water without surfactant as the reaction medium. Unlike the case of the L_3 silicate, when the xerogel was made, hydrolysis did not immediately proceed upon addition of TMOS, and agitation of the solution was necessary for the reaction to begin. A comparison of the SAXS from the silicate L_3 material and from a xerogel made without surfactant is shown in Fig. 3. Both samples had previously been vacuum dried for Brunauer-Emmett-Teller (BET) measurements (see below). A peak was observed for the silicate L_3 corresponding to a distance of 130 Å. In contrast, in the xerogel, there was no discernible SAXS peak; rather, the scattered intensity fell off monotonically as $q^{-3.8}$. The absence of a peak is most simply interpreted as a very wide variation in pore sizes. Although it is possible that there was a peak at too large a spacing to be resolved, this is unlikely because the silica volume fraction of the material was comparable to L_3 materials that did show a peak.

Although the gels produced here have been dried by evaporation and are therefore more accurately compared to xerogels, the bulk of the literature is on aerogels (dried by supercritical extraction) and that is where we will turn our attention, because gel formation is thought to be similar in both cases. In the formation of an aerogel, hydrolysis and polycondensation initially result in small silica particles 1 to 2 nm in diameter (*26*). Continued growth is through diffusion-limited aggregation of the initially formed particles into an open fibril structure. The hallmark of these structures is their fractal nature, which means that self-similar pore structure may be found on a wide variety of length scales. Indeed, SAXS analysis indicates that aerogels exhibit fractal-like correlations with asymptotic fall-offs that are proportional to q^{-4}, which represents the lower size cutoff of the relatively smooth parent particles. The diffraction from such a structure does not have a well-defined peak because no single pore size dominates (*26*). This diffraction corresponds exactly to the diffraction from our material (Fig. 3) made in the absence of surfactant.

In contrast, the L_3 phase has a dominant pore dimension that is readily controlled by the concentration of the original surfactant solution. Although there is some variation in the characteristic dimension, the polydispersity is small (because no loss of definition was observed for the peak), leading to the peak seen in Fig. 3. The major differences, therefore, between the silicate L_3 material and xerogels or aerogels are that the L_3 has two distinct, continuous, interpenetrating channel networks that traverse the entirety of the material (assuming that the topology of the silicate L_3 matches that of the original amphiphilic L_3), and the characteristic dimension in the silicate L_3 may be varied by changes in the concentration of the original solution. Measured surface areas for aerogels are in the same range, but in general at the upper end, as those measured for the silicate L_3 materials. Because of differences in structure between L_3 silicates and aerogels (fused tubes versus fused fibrils), it is likely that the L_3 silicate has more strength for the same density of silica. As is the case for xerogels and aerogels, silicate L_3 materials conform to the shape of the container in which they are made.

The silicate L_3 was further characterized by BET analysis and electron microscopy. The average surface area per volume was determined with a Micromeritics (Norcross, Georgia) Flowsorb 2300 single-point BET that used a He/N_2 (70/30) gas mixture to measure the surface area. Measurements were performed on uncalcined silicate L_3 materials formed with surfactant and on xerogels formed with acidified water only. Samples were vacuum-dried at 85°C and then degassed at 90°C until a consistent reading was obtained. The surface areas of the L_3 materials varied as a function of volume fraction between 375 and 525 m^2/g. Because the pores formed in the silicate L_3 materials are not a consequence of removal of surfactant but rather correlate to the aqueous channels in the phase, calcination of the samples was not required to obtain the surface area of the samples. Calcination to remove the surfactant would, however, open a third continuous pore network.

TEM was performed on samples that had already been used for BET measurements. Micrographs typical of all samples made from (i) the silicate L_3 phase and (ii) the xerogel made from acidified water are shown in Fig. 4. Samples were extensively studied under conditions of different defocus, and the features shown are characteristic for at least 95% of the area observed. Gross differences are immediately obvious: The silicate L_3 has distinct features and these features are seen for all volume fractions (that is, for samples with initial solvent compositions ranging from 40 to 95 weight %, albeit varying in length scale. In contrast, the xerogel has no distinctive features at all. A two-point pair-correlation function analysis performed on the silicate L_3 material showed that at distances above $\sim$2.5 nm, the system is completely random; that is, there is no defined length scale and no long-range correlation (*28*). An estimate of the pore size in the silicate L_3 phase may be obtained from this micrograph and correlates to $\sim$6 nm, which indicates that in this acid-synthesized silicate, the thickness of the silica walls, although uniform, is larger than 1 nm as measured under basic conditions (*21*).

Our results unambiguously distinguish between the silicate L_3 mesosphase and xerogels and aerogels. The major features distinguishing the silicate L_3 from other silica-surfactant mesophases are that it is nonperiodic yet contains well-defined silica wall thicknesses and monodisperse pore dimensions. Also, in addition to the fixed thickness pore that arises if the surfactant is removed, there are two other pore structures whose dimensions vary with the original solvent fraction and that can be adjusted to be much larger than the surfactant bilayer thickness. Silica L_3 materials may be fabricated into bulk monoliths that are devoid of grain boundaries. These novel characteristics open up new possibilities in the use of mesoporous materials in applications ranging from filtration media to the processing of nanostructured composites.

REFERENCES AND NOTES

1. C. T. Kresge *et al.*, *Nature* **359**, 710 (1992); J. S. Beck *et al.*, *J. Am. Chem. Soc.* **114**, 10834 (1992).
2. Q. Huo *et al.*, *Chem. Mater.* **6**, 1176 (1994); Q. Huo, R. Leon, P. M. Petroff, G. D. Stucky, *Science* **268**, 1324 (1995); Q. Huo, D. I. Margolese, G. D. Stucky, *Chem. Mater.* **8**, 1147 (1996); S. Schacht, Q. Huo, I. G. Voight-Martin, G. D. Stucky, F. Schüth, *Science* **273**, 768 (1996).
3. S. Mann, *Nature* **365**, 499 (1993); S. Mann *et al.*, *Science* **261**, 1286 (1993).
4. P. T. Tanev, M. Chibwe, T. J. Pinnavaia, *Nature* **368**, 321 (1994); P. T. Tanev and T. J. Pinnavaia, *Science* **267**, 865 (1995); *ibid.* **271**, 1267 (1996).
5. M. D. McGehee *et al.*, in *Proceedings of the 52nd Annual Meeting of the Microscopy Society of America*, G. W. Bailey and A. J. Garratt-Reed, Eds. (San Francisco Press, San Francisco, CA, 1994), pp. 448–449.
6. G. S. Attard, J. C. Glyde, C. G. Göltner, *Nature* **378**, 366 (1995).
7. H. Yang, N. Coombs, I. Sokolov, G. A. Ozin, *ibid.* **381**, 589 (1996).
8. I. A. Aksay *et al.*, *Science* **273**, 892 (1996).
9. H.-P. Lin and C.-Y. Mou, *ibid.*, p. 765.
10. P. V. Braun, P. Osenar, S. I. Stupp, *Nature* **380**, 325 (1996).
11. M. D. Alba, Z. Luan, J. Klinowski, *J. Phys. Chem.* **100**, 2178 (1996).
12. C.-G. Wu and T. Bien, *Science* **264**, 1757 (1994).
13. G. Porte, J. Marignan, P. Bassereau, R. May, *J. Phys. France* **49**, 511 (1988); R. Strey, W. Jahn, G. Porte, P. Bassereau, *Langmuir* **6**, 1635 (1990); G. Porte *et al.*, *J. Phys. II France* **1**, 1101 (1991); M. Skouri, J. Marignan, J. Appell, G. Porte, *ibid.*, p. 1121.
14. D. Gazeau, A. M. Bellocq, D. Roux, T. Zemb, *Europhys. Lett.* **9**, 447 (1989); M. E. Cates *et al.*, *ibid.* **5**, 733 (1988); D. Roux *et al.*, *ibid.* **11**, 229 (1990); S. T. Milner, M. E. Cates, D. Roux, *J. Phys. France* **51**, 2629 (1990); D. Roux, C. Coulon, M. E. Cates, *J. Phys. Chem.* **96**, 4174 (1992).
15. D. Anderson, H. Wennerström, U. Olsson, *J. Phys. Chem.* **93**, 4243 (1989).
16. B. Balinov, U. Olsson, O. Söderman, *ibid.* **95**, 5931 (1991).

17. C. Quilliet, M. Kléman, M. Benillouche, F. Kalb, *C. R. Acad. Sci. Ser. II* **319**, 1469 (1994); C. Quilliet, C. Blanc, M. Kléman, *Phys. Rev. Lett.* **77**, 522 (1996).
18. J. Daicic *et al.*, *J. Phys. II France* **5**, 199 (1995).
19. A. Maldonado, W. Urbach, R. Ober, D. Langevin, *Phys. Rev. E* **54**, 1774 (1996).
20. K. M. McGrath, *Langmuir* **13**, 1987 (1997).
21. A. Firouzi *et al.*, *Science* **267**, 1138 (1995).
22. R. A. Laudise and D. W. Johnson Jr., *J. Non-Cryst. Solids* **79**, 155 (1986).
23. R. Vacher, T. Woignier, J. Pelous, E. Courtens, *Phys. Rev. B* **37**, 10503 (1988).
24. J. Phalippou, T. Woignier, M. Prassas, *J. Mater. Sci.* **25**, 3111 (1990).
25. D. W. Schaefer *et al.*, *J. Non-Cryst. Solids* **145**, 105 (1992).
26. A. Emmerling and J. Fricke, *ibid.*, p. 113; P. Scheuerpflug, M. Hauck, J. Fricke, *ibid.*, p. 196.
27. D. Posselt, J. S. Pederson, K. Mortensen, *ibid.*, p. 128.
28. S. Torquato, unpublished results.
29. M. W. Tate, E. F. Eikenberry, S. M. Gruner, *Rev. Sci. Instrum.* **68**, 47 (1997).
30. Supported by the U.S. Army Research Office (grant DAAH04-95-1-0102), the U.S. Department of Energy (grant DE-FG02-87ER60522), and the Materials Research Science and Engineering Center program of NSF (grant DMR-940032).

A Di-Acidic Signal Required for Selective Export from the Endoplasmic Reticulum

Noriyuki Nishimura and William E. Balch*

Transport of membrane proteins between intracellular compartments requires specific sequences in the protein cytoplasmic domain to direct packaging into vesicle shuttles. A sequence that mediates export from the endoplasmic reticulum (ER) has proved elusive. A di-acidic signal (Asp-X-Glu, where X represents any amino acid) on the cytoplasmic tail of vesicular stomatitis virus glycoprotein (VSV-G) and other cargo molecules was required for efficient recruitment to vesicles mediating export from the ER in baby hamster kidney cells. The existence of such a signal provides evidence that export from the ER occurs through a selective mechanism.

Vesicular transport of proteins between intracellular compartments is coordinated by the activity of coat complexes that direct the selection of cargo through cytoplasmic signals and budding from membranes (*1, 2*). These coat complexes include clathrin, which mediates sorting of receptors containing Tyr-based motifs from the trans-Golgi network and the cell surface (*3*); COPI, which binds di-lysine motifs and functions to direct retrograde transport of proteins from pre-Golgi and Golgi compartments (*4, 5*); and COPII, which participates in protein export from the ER (*1*). A signal that directs recruitment of proteins to COPII-coated vesicles remains to be defined.

VSV-G is a type 1 transmembrane protein that forms a homotrimer (*6*). It has a 29–amino acid oligomer (29-mer) cytoplasmic tail at its COOH-terminus that may be important for ER export (*7*). Consistent with this possibility, we found that addition of a 29-mer cytoplasmic tail peptide to an in vitro ER to Golgi transport assay in baby hamster kidney (BHK) cells inhibited VSV-G transport in a dose-dependent manner (Fig. 1A). We also analyzed the transport of truncated VSV-G mutants in vivo with a vaccinia virus transient expression system. A mutant lacking the entire 29–amino acid cytoplasmic tail of VSV-G is defective in folding and oligomerization (*7*) and exits the ER very slowly (Fig. 1B). In

contrast, a mutant lacking 26 amino acids of the cytoplasmic tail is not defective in folding or oligomerization (*7*), yet is also exported at a reduced rate (Fig. 1B).

To locate the region in the COOH-terminal 26 amino acids responsible for ER export, we generated a series of truncation mutants (Fig. 1C). Deletion of the COOH-terminal five amino acids had no effect on ER to Golgi transport at the 20-min time point, whereas removal of eight amino acids reduced transport by nearly 80% (Fig. 1C). Deletion of residues 1 to 9 or 6 to 13 had no effect, whereas deletion of residues 1 to 13 showed a partial decrease in transport efficiency (Fig. 1C). Deletion of residues 14 to 24 reduced transport to the amount observed for the residue 4 through 29 deletion (del 4-29) truncation (Fig. 1C). These results demonstrate that a spacer region from

the membrane is necessary to present a signal critical for ER export that resides within residues 14 to 24.

To identify specific residues required for transport, we substituted amino acid residues 14 to 24 individually with Ala. The Ala scan revealed that neither the Tyr nor Ile residues, which are critical for basolateral sorting (Fig. 1C) (*8*), were required for ER export. Rather, two acidic residues, the Asp at position 21 (D21) and the Glu at position 23 (E23) (Fig. 2A), when mutated individually or in combination, reduced the rate of ER to Golgi transport to that observed for the del 4-29 construct (*9*). The requirement for the DXE sequence was specific because mutation of D21 to E or R, or E23 to D or R, also caused reduced export (Fig. 2A). Examination of transport over a longer time course (Fig. 2B) revealed that the transport defect resulting from mutation of the di-acidic motif predominantly affected the rate of export; the extent of transport was less strongly affected at later time points. The decreased rate of transport correlated with a reduced rate of VSV-G export from the ER as detected by indirect immunofluorescence. Wild-type VSV-G had a prominent Golgi distribution at the 10-min time point, whereas a double mutant in which the DXE signal was mutated to AXA remained localized to the ER (Fig. 2C). ER export of the double mutant appeared to occur through a COPII-mediated pathway (*2, 10*) because VSV-G transport remained completely sensitive to Sar1 mutants that block the assembly of COPII

Table 1. Alignment of the DXE motif found in the cytoplasmic domain of transmembrane proteins. Sequences were obtained from the National Center for Biotechnology Information (NCBI). Asialoglycoprotein receptor, ASGPR; varicella zoster virus glycoprotein I, VZV GPI. The Yxxφ motifs are underlined. The acidic residues conforming to the di-acidic signal (DXE) involved in ER export are highlighted in bold. Proteins containing a more general (D/E)X(E/D) signal found on the COOH-terminal side of a Yxxφ motif are listed in (*27*).

Protein	NCBI identifier	Sequence
VSV-G*	Virus (138311)	TM-18aa-<u>YTD</u>**I**E MNRLGK
LAP*	Human (130727)	TM-8aa-<u>YRHVA</u>**DGE**DHA
CD3δ	Mouse (115986)	TM-21aa-<u>YQPLR</u>**DRE**DTQ-14aa
CD3γ	Mouse (115994)	TM-21aa-<u>YQPLK</u>**DRE**YDQ-12aa
ASGPR H1 subunit	Human (126132)	MTKE<u>YQDL</u>QHL**DNE**ES-24aa-TM
VZV GPI	Virus (138246)	TM-20aa-<u>YAGL</u>PVD**DFE**DSESTDTEEEF
E-cadherin	Human (399166)	TM-95aa-<u>YDSL</u>LVF**DYE**GSGS-42aa
CD3ε (Y177E)*	Mouse (1345709)	TM-35aa-<u>YEPI</u>RKGQR**D**L(<u>Y</u> → **E/D**)<u>SGL</u>NQRAV

*Proteins with known functional di-acidic exit signals.

Departments of Molecular and Cell Biology, The Scripps Research Institute, 10550 North Torrey Pines Road, La Jolla, CA 92037, USA.

*To whom correspondence should be addressed. E-Mail: webalch@scripps.edu